ELEMENTA
Science of the Anthropocene

Assessment of the sea-ice carbon pump: Insights from a three-dimensional ocean-sea-ice-biogeochemical model (MPIOM/HAMOCC)

R. Grimm[1*] • D. Notz[1] • R.N. Glud[2,3,4,5] • S. Rysgaard[5,6,7,8] • K.D. Six[1]

[1]Max Planck Institute for Meteorology, Hamburg, Germany
[2]Department of Biology, University of Southern Denmark, Odense, Denmark
[3]Nordic Center for Earth Evolution, University of Southern Denmark, Odense, Denmark
[4]Scottish Association for Marine Science, Oban, United Kingdom
[5]Arctic Research Centre, Aarhus University, Aarhus, Denmark
[6]Centre for Earth Observation Science, Department of Environment and Geography, University of Manitoba, Winnipeg, Canada
[7]Department of Geological Sciences, University of Manitoba, Winnipeg, Canada
[8]Greenland Climate Research Centre, Greenland Institute of Natural Resources, Nuuk, Greenland

*rosina.grimm@mpimet.mpg.de

Abstract

It has been suggested that geochemical processes related to sea-ice growth and melt might be important for the polar carbon cycle via the so called sea-ice carbon pump (SICP). The SICP affects the air-sea CO_2 exchange by influencing the composition of dissolved inorganic carbon (DIC) and total alkalinity (TA) in the surface ocean. Here we quantify the strength of the SICP-induced air-sea CO_2 flux using the global three-dimensional ocean-sea-ice-biogeochemical model MPIOM/HAMOCC. Simulations prescribing the range of observed DIC and TA concentrations in the sea ice were performed under two idealized climate scenarios for the present-day and the future oceanic and sea-ice state, both forced with a fixed atmospheric CO_2 concentration. Model results indicate that the SICP-induced air-sea CO_2 uptake increases with higher ratios of TA:DIC prescribed in the sea ice relative to the basic oceanic TA:DIC ratios. Independent of the modeled scenario, the simulated strength of the SICP is larger in the Antarctic than in the Arctic, because of more efficient export of brine-associated DIC from the Antarctic mixed layer. On an annual basis, we generally find an enhanced SICP-induced oceanic CO_2 uptake in regions with net sea-ice melt, and enhanced SICP-induced oceanic CO_2 out-gassing in regions with net sea-ice growth. These general regional patterns are modified further by the blockage of air-sea gas exchange through sea-ice coverage. Integrated over the sea-ice zones of both hemispheres, the SICP-induced oceanic CO_2 uptake ranges from 2 to 14 Tg C yr^{-1}, which is up to 7% of the simulated net CO_2 uptake in polar regions, but far less than 1% of the current global oceanic CO_2 uptake. Hence, while we find that the SICP plays a minor role in the modern global carbon cycle, it is of importance for the regional carbon cycle at high latitudes.

Domain Editor-in-Chief
Jody W. Deming,
University of Washington

Associate Editor
Lisa A. Miller,
Fisheries and Oceans Canada

Knowledge Domain
Ocean Science

Article Type
Research Article

Part of an *Elementa* Special Feature
Biogeochemical Exchange Processes at Sea-Ice Interfaces (BEPSII)

Received: February 15, 2016
Accepted: October 6, 2016
Published: November 17, 2016

1. Introduction

The magnitude of CO_2 exchange between the atmosphere and the ocean is determined by the difference in partial pressure of CO_2 (pCO_2) between the two reservoirs. This difference is affected by at least three oceanic pumps that carry carbon from the ocean surface to greater depths: the solubility pump, the biological pump, and the carbonate counter pump (e.g., Sarmiento and Gruber, 2006). In addition to these three carbon pumps, recent studies have suggested that processes related to sea-ice growth and melt may also

affect the air-sea CO_2 exchange (Rysgaard et al., 2007, 2009, 2011; Dieckmann et al., 2010; Loose et al., 2011). However, a robust quantification of this so-called sea-ice carbon pump (SICP) has been lacking so far. This study quantifies the contribution of the SICP to air-sea CO_2 exchange in the state-of-the-art global ocean-sea-ice biogeochemistry model MPIOM/HAMOCC.

The basic functioning of the SICP can be understood as follows. During sea-ice growth, all dissolved tracers, including dissolved inorganic carbon (DIC) and the total alkalinity (TA, the acid neutralization capacity of seawater), are concentrated in the brine. Hence, when drainage of brine into the ocean occurs, it reduces the content of tracers in the bulk sea ice and increases their content in the underlying ocean. Simultaneously, the precipitation of the carbonate crystal ikaite ($CaCO_3(s) \cdot 6H_2O$),

$$Ca^{+2} + 2HCO_3^- + 5H_2O \rightarrow CaCO_3(s) \cdot 6H_2O + CO_2(aq),$$

can occur within the sea-ice brine, as observed in both natural and artificial sea ice (Dieckmann et al., 2008, 2010; Rysgaard et al., 2012, 2013, 2014; Geilfus et al., 2013). Because one mole of DIC is consumed and TA decreases by two moles for each mole of ikaite formed, ikaite crystals have a TA:DIC ratio of 2:1 (for details on the carbonate chemistry see, e.g., Sarmiento and Gruber, 2006). If the formed ikaite crystals remain in the ice matrix while some of the $CO_2(aq)$ produced during ikaite formation is rejected via brine drainage to the underlying ocean, then a TA:DIC ratio between 1 and 2 remains in the bulk sea ice. This ratio can be further modified through other biogeochemical processes such as the growth of sea-ice algae. During sea-ice melt, the release of melt-water to the ocean dilutes the oceanic TA and DIC concentrations, and the dissolution of ikaite potentially increases the oceanic TA:DIC ratio which is usually 1.1.

These changes in the surface ocean TA and DIC affect the oceanic pCO_2 and determine the direction and strength of the SICP-induced air-sea CO_2 flux (Figure 1). If, on average, the polar mixed layer becomes enriched in brine-associated TA and DIC of potentially low TA:DIC ratio, then a SICP-induced flux of CO_2 to the atmosphere can be expected. Such CO_2 flux to the atmosphere would occur, for example, in regions with a net export of sea ice or where the oceanic circulation causes a net import of brine-associated TA and DIC to the mixed layer. On the other hand, if melt-water dilutes the DIC and TA concentrations in the mixed layer potentially accompanied by an increase in the mixed layer TA:DIC ratio due to the dissolution of ikaite, then a SICP-induced oceanic uptake of atmospheric CO_2 can be expected. Such CO_2 uptake by the ocean would occur, for example, in regions with a net import of sea ice or where the oceanic circulation transports brine-associated TA and DIC away from the mixed layer. Hence, the total SICP-induced oceanic CO_2 uptake will increase with the fraction of brine being exported from the polar mixed layer (Rysgaard et al., 2007).

Budget calculations of the potential size of the SICP-induced annual mean CO_2 flux have suggested a possible maximum oceanic uptake of 9 to 20% (14 to 31 Tg C yr^{-1}) of the current net uptake in the region north of 62°N, and 42 to 116% (19 to 52 Tg C yr^{-1}) of the current net uptake in the region south of 50°S (Rysgaard et al., 2011). Including an idealized representation of the SICP in our prognostic three-dimensional global ocean-sea-ice-biogeochemical model allows us to evaluate the robustness of these estimates in a more comprehensive setup.

To do so, we analyzed the impact of sea-ice thermodynamics and dynamics and of oceanic circulation on the magnitude of the SICP-induced air-sea CO_2 exchange. We considered two idealized equilibrium climate scenarios with fixed atmospheric CO_2 concentrations: (i) a climate state representing the present-day oceanic and sea-ice state; and (ii) a climate with reduced Arctic sea-ice extent and volume and reduced strength of

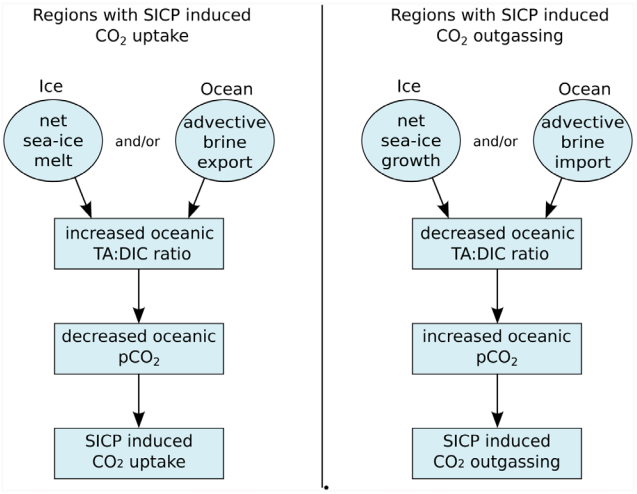

Figure 1

Schematic of the main mechanisms determining the direction of the SICP-induced air-sea CO_2 flux.

doi: 10.12952/journal.elementa.000136.f001

the oceanic overturning circulation. These scenarios allowed us to disentangle the various contributors to the overall magnitude of the SICP. Because of the high spatial and temporal variability in the observed sea-ice TA and DIC concentrations, we ran several simulations for each climate scenario using different prescribed ratios and concentrations of TA and DIC in the sea ice that cover the observed range. This study complements a related study that is based on the model NEMO-LIM-PISCES and quantifies the SICP under pre-industrial climate conditions (Moreau et al., 2016).

2. Methods

2.1 Ocean–sea-ice–biogeochemical model

Our model simulations were performed using the Max Planck Institute global ocean-sea-ice general circulation model MPIOM (Marsland et al., 2003; Jungclaus et al., 2013) coupled to the Hamburg ocean carbon cycle model HAMOCC (Maier-Reimer et al., 2005; Ilyina et al., 2013). MPIOM is a free surface model with hydrostratic and Boussinesq assumptions. The model computes isopycnal diffusion of the thermohaline fields. Tracer transport by unresolved eddies is parameterized following Gent et al. (1995). MPIOM includes a sea-ice model (Marsland et al., 2003; Notz et al., 2013) formulated with a viscous-plastic rheology following Hibler (1979). MPIOM is formulated on an orthogonal C-grid in the horizontal and z-grid in the vertical. In the setup used in this study one pole is located over Greenland and the other over Antarctica. The horizontal resolution (GR15) is 1.5°, which corresponds to about 12 km around the poles and 150 km in the tropics. The time-step of the model is set to 1.2 hours. The water column is divided into 40 levels in the vertical, 9 of which are in the uppermost 100 m, and 18 in the uppermost 500 m.

HAMOCC is a state-of-the-art ocean carbon cycle model resolving oceanic and sedimentary organic and inorganic carbon processes and therefore includes the biological pump, the carbonate counter pump, and the solubility pump (Six and Maier-Reimer, 1996; Heinze and Maier-Reimer, 1999; Heinze et al., 1999; Ilyina et al., 2013). The temporal evolution of TA and DIC is computed prognostically. All biogeochemical tracers of HAMOCC are transported with the same advection scheme as the thermohaline fields of MPIOM.

The air-sea CO_2 flux, F, in HAMOCC is derived at each time step by computing the pCO_2 difference between the atmosphere and the uppermost oceanic layer, ΔpCO_2, multiplied by a gas transfer velocity, k, the solubility of CO_2, α, according to Weiss (1974), and the open-water fraction, A_{op}, as gas exchange is assumed to occur only in the open-water part of the grid cell. Hence,

$$F = k\,\alpha\,A_{op}\,\Delta pCO_2,$$

where k depends on the Schmidt number (Gröger and Mikolajewicz, 2011) and wind speed at the surface (Wanninkhof, 1992). The oceanic pCO_2 in the model is computed as a function of temperature, salinity, DIC, TA, and sea-level pressure. More details on the biogeochemical processes simulated in HAMOCC are given by Six and Maier-Reimer (1996) and Ilyina et al. (2013).

2.1.1 Treatment of brine and tracer release

To simulate the SICP including the formation of ikaite, we prescribed the mass concentration of dissolved tracers (solute) in sea ice (e.g., salinity, TA, DIC) as a constant value $C_{sol,ice}$ [g kg^{-1}]. The solute concentration change in the surface ocean $\Delta C_{sol,oce}/\Delta t$ [g kg^{-1} s^{-1}] from changes in ice mass was computed as

$$\Delta C_{sol,oce} / \Delta t = \frac{-\Delta m_{sol,oce} / \Delta t}{m_{seawater}} = \frac{C_{sol,ice}\Delta m_{ice} / \Delta t}{z\rho_{seawater}}.$$

Here $\Delta m_{sol,oce}/\Delta t$ denotes the rate of change of the mass of a dissolved tracer in seawater [g s^{-1}], $m_{seawater}$ denotes the mass of seawater [kg], $\rho_{seawater}$ denotes seawater density [kg m^{-3}], z denotes the thickness of the surface ocean layer [m], and $\Delta m_{ice}/\Delta t$ denotes the gross sea-ice growth rate (positive values) and melt rate (negative values) [kg m^{-2} s^{-1}]. Hence, with a constant tracer concentration prescribed in the sea ice, growth of sea ice leads to an increase of the oceanic tracer concentration, while melt leads to a decrease of oceanic tracer concentration. Within each time step, Δt (1.2 h), the model computes the thermodynamics of sea ice (i.e., growth and melt) and the dynamics of sea ice (i.e., convergence and divergence). In the model, sea-ice salinity is set to a constant value of 5 g kg^{-1}, which results in a distribution of modeled water masses and large-scale circulation features that are in good agreement with observations (Jungclaus et al., 2013), even though open ocean convection in the Southern Ocean might be too strong (Stössel et al., 2015).

2.2 Model initialization and boundary conditions

The model was initialized from the oceanic, sea-ice and biogeochemical fields obtained from the year 1979 of the fifth phase of the Coupled Model Intercomparison Project (CMIP5) using the Max-Planck-Institute for Meteorology's Earth System Model (MPI-ESM) in GR15/L40 (1.5°) resolution (Ilyina et al., 2013).

We ran a spin-up simulation of 920 years by forcing the model each year with daily heat, freshwater and momentum fluxes computed from the OMIP climatological atmospheric forcing (Röske, 2006). To correct for the unbalanced globally integrated surface freshwater flux and other errors in the forcing fields of precipitation and river runoff, surface salinity is restored with a time-linear relaxation coefficient of $3.3{\cdot}10^{-7}$ s^{-1} to the conditions derived from the Polar Science Center Hydrographic Climatology (PHC2, which is based on the climatology provided by Levitus et al. (1998), with modifications in the Arctic based on Steele et al. (2001)). The atmospheric CO_2 concentration was kept constant at the level at the end of the year 1979 (337.4 ppm) throughout the spin-up simulation.

The spin-up simulation reaches quasi-equilibrium concerning deep-water salinity and temperature, the meridional overturning circulation, the sea-ice state, and the air-sea CO_2 flux after 700 years of simulation, and was continued until the year 920.

2.3 Experimental design

To identify the influence of climatic changes on the strength of the SICP, we simulated two idealized climate scenarios (Section 2.3.1). For both idealized climate scenarios, we performed several simulations with different prescribed TA and DIC concentrations in the sea ice, spanning the range of observed values (Section 2.3.2). All simulations were initialized at the end of the spin-up simulation, and were run for 500 years of simulation.

2.3.1 Idealized climate scenarios

In the equilibrium (EQ) scenario, which roughly represents today's physical forcing on the ocean and atmosphere with fixed atmospheric CO_2 concentrations, we forced the model with the OMIP atmospheric forcing as used in the spin-up simulation.

In the global warming (WARM) scenario, we forced the model with a warming climate, while the atmospheric CO_2 concentration is kept constant at 337.4 ppm as in the EQ scenario. As we used an ocean-only model, we needed to provide forcing fields for the WARM scenario. To obtain these, we first computed the climatological anomaly of each field between the last 30 years of the 1000 year long CMIP5 control experiment and the climatological mean of the years 66 to 95 of the CMIP5 experiment with an increase in atmospheric CO_2 concentration of 1% yr^{-1}, calculated both using MPI-ESM (Ilyina et al., 2013). By adding these anomaly fields to the climatological fields of the OMIP forcing, we generate a 'new' forcing. This 'new' forcing was applied in the WARM scenario by linearly increasing the added anomaly over the first 65 years of the simulation from zero to the full anomaly, at which level it is then kept constant until the end of the 500 year model run. The same anomaly forcing was applied to sea-surface salinity relaxation in the WARM scenario. We further note that an ocean-only model implies no feedback from ocean processes to the atmospheric climate.

2.3.2 SICP parameter setting

For each idealized climate scenario, we used a constant sea-ice TA:DIC of 2000:2000 mmol m^{-3} as our control parameter setting (Table 1). This control parameter setting is very similar to standard oceanic conditions, and thus minimizes fractionation of DIC and TA, and consequently oceanic pCO_2 changes, upon sea-ice growth and melt. The impact of the SICP can then readily be evaluated by assessing changes that occur for more realistic settings for TA and DIC relative to this control setting. The individual simulations were designed to cover the range of observed concentrations and ratios of TA:DIC in the sea ice (Table 1; Rysgaard et al., 2007, 2009, 2013; Fransson et al. 2011; Geilfus et al. 2013). In addition to these observed parameter settings, we also performed simulations with a parameter setting of both TA and DIC at zero in the sea ice, as this setting is the default setup in most ocean-sea-ice biogeochemical models, including MPIOM/HAMOCC (e.g., Steiner et al., 2014, and models and citations therein). Upon sea-ice growth and melt, this setup does

Table 1. Summary of the performed model experiments

Type of experiment	Prescribed sea-ice TA:DIC concentrations (mmol m^{-3}:mmol m^{-3})	Name of experiment[a]	
Control	2000:2000	EQ_CTRL	WARM_CTRL
SICP	0:0	EQ_R0	WARM_R0
	800:400	EQ_R2h	WARM_R2h
	800:727	EQ_R1.1h	WARM_R1.1h
	100:50	EQ_R2l	
	100:91	EQ_R1.1l	

[a]EQ indicates idealized climate scenario of present-day physical climate with fixed atmospheric CO_2 concentration; WARM indicates idealized climate scenario with potential future global warming and fixed atmospheric CO_2 concentration; CTRL indicates control; R is the sea-ice TA:DIC ratio (where R0 indicates both concentrations set to 0, R1.1 indicates a ratio of 1.1, and R2 a ratio of 2); and h versus l indicate high versus low concentrations of TA and DIC.

doi: 10.12952/journal.elementa.000136.t001

not change the oceanic TA:DIC ratio but simulates full drainage of brine-associated TA and DIC into the ocean upon sea-ice growth and full dilution of oceanic TA and DIC by melt water. For our experiments we follow a naming scheme that is detailed in Table 1.

2.4 Quantification of the SICP

Within each simulated, idealized climate scenario the circulation fields of the SICP experiments are identical, and the changes due to biological production are insignificant (Text S1, Figure S1). Correspondingly, in each idealized climate scenario the effect of the SICP-induced changes in ocean properties, e.g., the air-sea CO_2 flux, can be separated by examining differences between simulations with different SICP parameter settings. We quantified the changes in biogeochemical properties induced by the SICP by subtracting within each idealized climate scenario the simulation results based on the control parameter setting (CTRL) from the simulation results based on the SICP parameter settings. The differences are denoted by "Δ"; e.g., ΔEQ_R2h denotes EQ_R2h minus EQ_CTRL (where R2h refers to a TA:DIC ratio of 2 with high tracer concentrations; Table 1).

2.5 Determination of oceanic brine and melt-water distribution

SICP-induced changes in TA can be used to illustrate the footprints of brine and melt-water in the ocean, as TA is not influenced by gas-exchange processes and changes to the SICP due to biological production are not significant (Text S1, Figure S1). We analyzed SICP-induced TA changes between the CTRL and R0 experiments in both the EQ scenario and the WARM scenario. In this analysis, a positive SICP-induced change in oceanic TA indicates that the increase of TA from local brine release and/or from oceanic transport of brine is larger than the decrease of TA from local sea-ice melt and/or from the oceanic transport of sea-ice melt-water. In the following, we refer to such a positive SICP-induced change in oceanic TA as "brine footprint", and to a negative SICP-induced change in oceanic TA as "melt-water footprint".

3. Results

3.1 Sea-ice volume

In the Arctic, the simulated sea-ice extent in the EQ scenario is in good agreement with the observational data of the National Oceanic and Atmospheric Administration (NOAA)/National Snow and Ice Data Center (NSIDC) (Meier et al., 2011). The Arctic sea-ice volume in the EQ scenario approximates the years 1963 to 2000 of the CMIP5 historical MPI-ESM runs (Notz et al., 2013; Figure 2a). In the Antarctic, the model underestimates the observed sea-ice extent, in particular during summer, resulting in a minimum simulated sea-ice volume that is close to zero in both idealized climate scenarios (Figure 2b). This underestimation is a known bias of MPIOM (Marsland et al. 2003; Jungclaus et al. 2013).

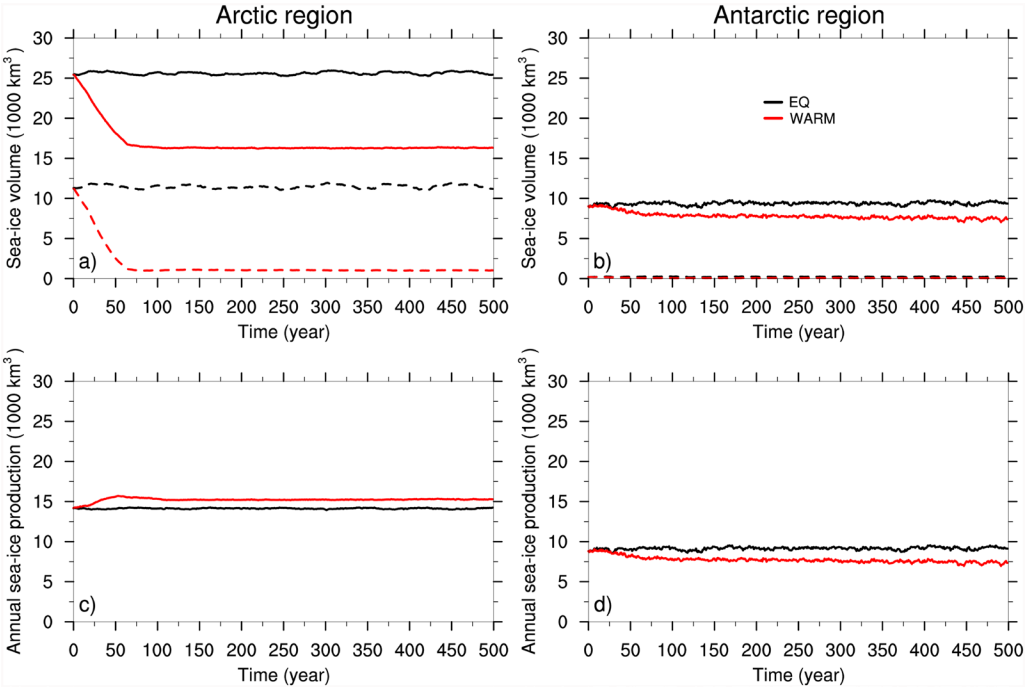

Figure 2

Simulated annual sea-ice volume and production over 500 years.

Annual maximum (solid lines) and minimum (dashed lines) sea-ice volume (1000 km^3) derived from monthly mean values of the EQ scenario (black lines) and WARM scenario (red lines) for the Arctic (a) and Antarctic region (b); annual sea-ice production (1000 km^3) for the Arctic (c) and Antarctic region (d) derived by subtracting the annual minimum from the annual maximum sea-ice volume.

doi: 10.12952/journal.elementa.000136.f002

Compared to the EQ scenario, the WARM scenario exhibits a continuous reduction of both the summer and winter sea-ice volume during the first 65 years of simulation in both hemispheres, which subsequently equilibrate at lower volumes (red lines in Figure 2a,2b). This evolution of sea-ice volume in both hemispheres is a direct consequence of the warming applied in the WARM scenario, which after 65 years of simulation is kept constant. In the WARM scenario, the annual sea-ice production is enhanced by 8% in the Arctic and reduced by 20% in the Antarctic compared to the EQ scenario (Figure 2c,2d). The Arctic sea-ice volume of the WARM scenario stabilizes at similar levels to those obtained in MPI-ESM by the end of the century in the CMIP5 RCP4.5 scenario (Notz et al., 2013).

3.2 Annual net sea-ice growth and melt

In both idealized climate scenarios on an annual mean, sea ice melts along the sea-ice margins and grows in the ice interior in both hemispheres (Figure 3). In the WARM scenario, the position of the Arctic sea-ice margin retreats northward relative to the EQ scenario (Figure 3a, 3c). In addition, in the WARM scenario over larger areas of the central Arctic Ocean, the actual annual sea-ice production is increased but the annual net sea-ice growth is reduced compared to the EQ scenario (Figure 1c). This reduction is because in the WARM scenario the sea ice grown in the central Arctic is also melted within this basin, and less efficiently exported southward than in the EQ scenario. In contrast, the Antarctic annual mean position of the sea-ice margin and regions of annual net sea-ice growth and melt barely change between the EQ scenario and the WARM scenario (Figure 3b and 3d).

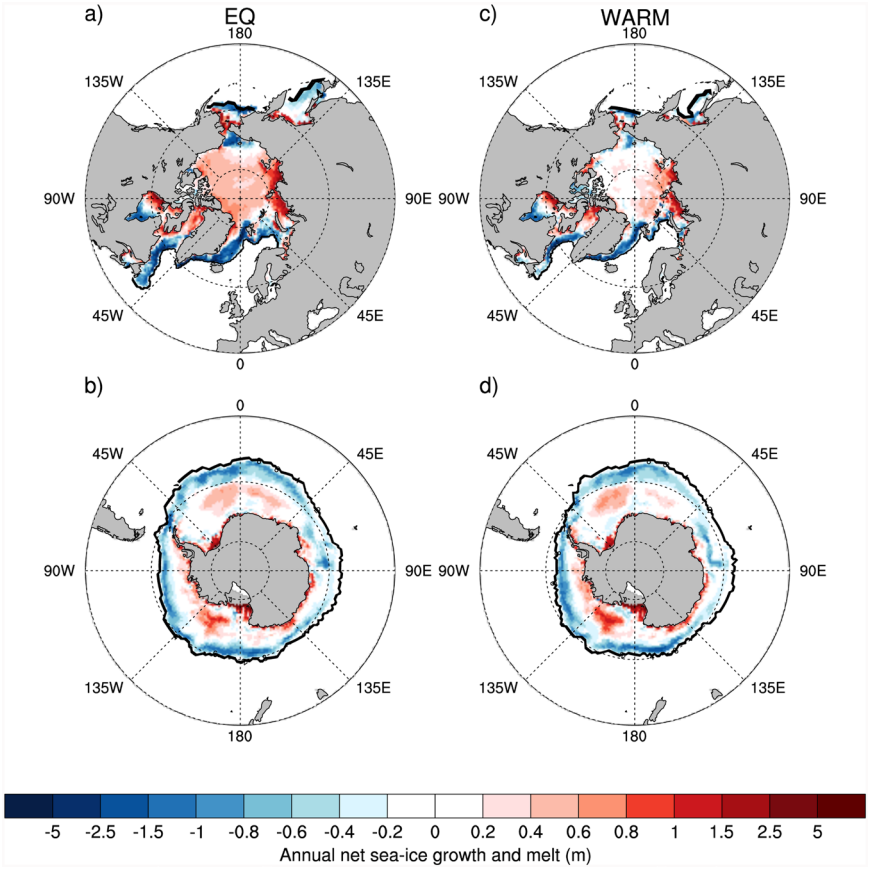

Figure 3

Simulated annual net sea-ice growth and melt.

Annual net sea-ice growth (positive values, red) and melt (negative values, blue) (m) in the EQ climate scenario (a,b), and the WARM climate scenario (c,d). The black lines indicate the annual mean position of the sea-ice margins. Latitudinal bands are shown for 80˚, 60˚ and 40˚. Results are averaged over the simulation years 451 to 500. Note that the color scale is nonlinear.

doi: 10.12952/journal.elementa.000136.f003

3.3 Mixed layer depth

Deep mixing occurs in the Labrador Sea and also to some extent in the Greenland Sea in the EQ scenario (Figure 4a). In the WARM scenario, the warmer climate reduces the mixed layer depth in the North Atlantic compared to the EQ scenario (Figure 4c). Similarly, the winter mixed layer depth is reduced in the central Arctic Ocean in the WARM scenario compared to the EQ scenario. In the Southern Ocean, very deep mixing occurs in the Weddell and Ross Seas in both the EQ scenario and the WARM scenario (Figure 4b and 4d). This open ocean deep mixing in the Southern Ocean is likely overestimated by the model, while dense-water formation on the shelves around Antarctica is underestimated (e.g., Marsland et al., 2004; Jungclaus et al., 2013; Stössel et al., 2015). Any uncertainty in the modeled location and strength

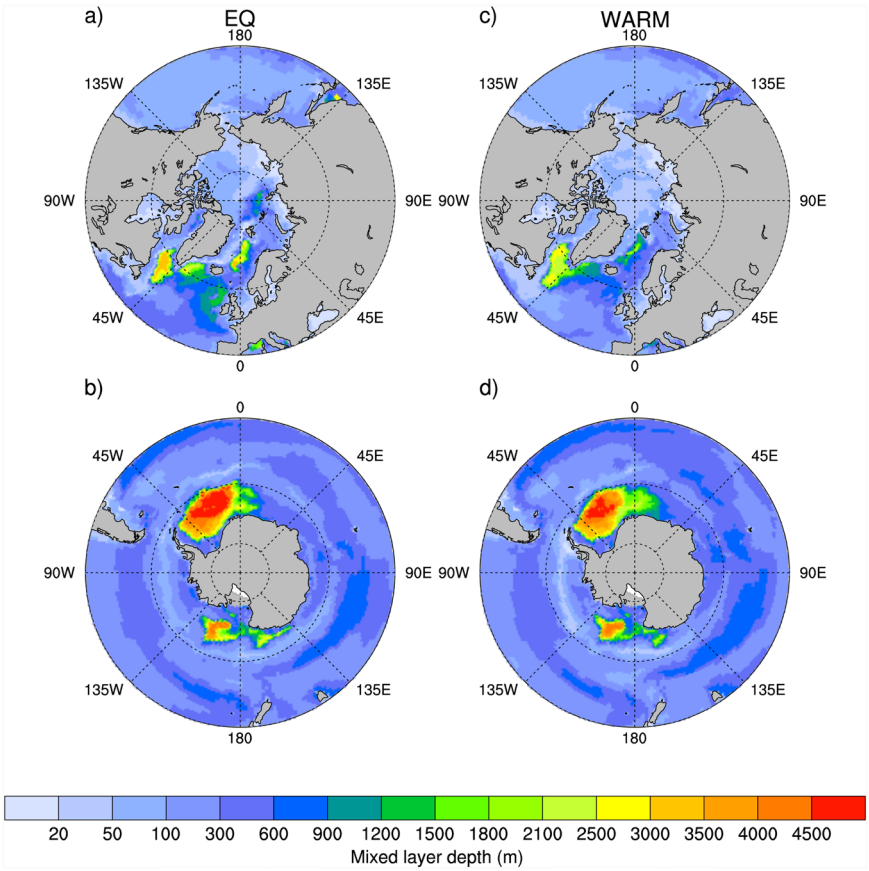

Figure 4

Simulated mixed layer depth.

Results for the mean mixed layer depth (m) in the EQ_ climate scenario (a,b) and the WARM climate scenario (c,d) for the Arctic region in March (a,c) and the Antarctic region in September (b,d). The mixed layer depth is diagnosed in the model as the depth where the potential density is 0.125 kg m^{-3} larger than at the surface. Latitudinal bands are shown for 80°, 60° and 40°. Results are averaged over the simulation years 451 to 500. Note that the color scale is nonlinear.

doi: 10.12952/journal.elementa.000136.f004

of dense-water formation might be relevant for the strength of the SICP-induced air-sea CO_2 flux. As for the northern hemisphere, in the WARM scenario deep mixing is reduced compared to the EQ_scenario, particularly in the Weddell Sea.

3.4 Meridional overturning stream function

The meridional overturning circulation is characterized by a clockwise rotating cell above 3000 m depth and north of 35°N, which is driven by the sinking of dense water in the North Atlantic Ocean (Figure 5b). Dense-water sinking in the Southern Ocean drives a counterclockwise rotating cell adjacent to Antarctica, and at depth below 3000 m (Figure 5a and 5b). The model simulates a maximum southward transport in the Atlantic Ocean of about 20 Sv (1 Sv = 10^6 m^3 s^{-1}) at 40°N, and 12 Sv at 60°N for the EQ_scenario (Figure 6). In the WARM scenario, the strength of the southward transport continuously weakens during the first 65 years of changing forcing to a minimum of 13 Sv at 40°N and 6 Sv at 60°N (Figure 6). While at 40°N the southward transport recovers during the period of constant forcing (years 65 to 500) to the initial strength of about 20 Sv after 120 years of simulation, at 60°N the recovery of the strength of the southward transport is much slower (Figure 6), and the transport is still around 3 to 4 Sv weaker than in the EQ_ scenario after 500 years of simulation (Figure 5d, Figure 6). Similarly, the strength of the counterclockwise rotating cell adjacent to Antarctica, and at depth below 3000 m, is reduced in the WARM compared to the EQ_scenario (Figure 5c). Any change in the meridional overturning circulation might influence the brine export into the deep ocean, and thus the strength of the SICP-induced air-sea CO_2 flux.

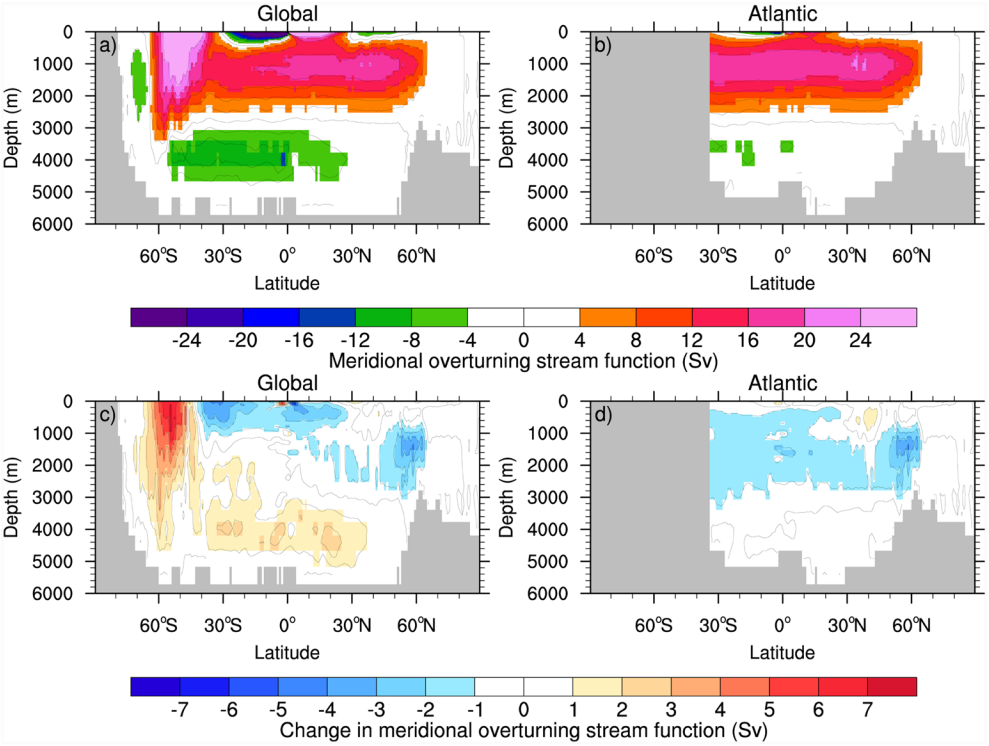

Figure 5

Simulated meridional overturning stream function.

Annual mean meridional overturning stream function (Sv) in the EQ climate scenario (a,b), where positive values indicate clockwise circulation, and change in the meridional overturning stream function in the WARM climate scenario relative to the EQ scenario (c,d). The panels show results for the global ocean (a,c) and the Atlantic Ocean (b,d). All results are averaged over the simulation years 451 to 500.

doi: 10.12952/journal.elementa.000136.f005

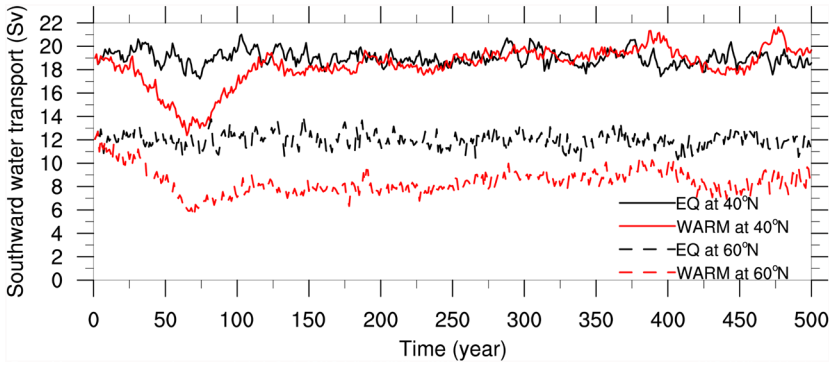

Figure 6

Simulated North Atlantic Ocean southward water transport.

Time series of the annual mean maximum for southward water transport (Sv) at 40°N (solid lines) and at 60°N (dashed lines) in the EQ climate scenario (black lines) and the WARM climate scenario (red lines).

doi: 10.12952/journal.elementa.000136.f006

3.5 Distribution of brine and sea-ice melt-water in the ocean

To analyze the distribution of brine and melt-water footprints, we examined the last 50 years of simulation, when the SICP-induced change in TA is stable in both the EQ scenario and the WARM scenario (Figures S2 and S3).

3.5.1 EQ scenario

A prevailing brine footprint in the surface ocean (positive SICP-induced change in TA) is simulated in areas of net sea-ice growth in the interior of the ice pack, and a melt-water footprint (negative SICP-induced change in TA) is simulated in net sea-ice melt areas along and partly beyond the sea-ice margins in both hemispheres (Figure 3a, 3b; Figure 7a, 7b). Generally the strength of the simulated brine footprint increases with net sea-ice growth, and the melt-water footprint increases with net sea-ice melt, although ocean circulation can modify these regional patterns (Figure 3a, 3b; Figure 7a, 7b). One prominent regional modification is simulated in the Beaufort Gyre; here the brine footprint is larger in the center of the gyre than along the coast of the Beaufort Sea (Figure 7a), although net sea-ice growth is larger along the coast (Figure 3a). This difference is because the Beaufort Gyre causes convergence towards its center, and hence a trapping of brine in the center of the gyre. At depth, the brine footprint is traceable to intermediate depth (about 350 m) in the Arctic, locally reaching as deep as 900 m in the Beaufort Sea and 2200 m in the Baffin Bay (not shown in detail; Figure 8a). The North Atlantic Ocean to a depth of 3500 m is characterized by a prevailing melt-water footprint, indicating that brine contribution to dense-water formation and its spreading into the North Atlantic Ocean is low in the model. In the Southern Ocean, on a zonal mean the brine footprint is transported from the upper ocean (south of 60°S) into the deep Pacific and Indian Ocean (below 2500 m depth) and into the deep Atlantic Ocean (below 3500 m depth) as far north as 55°N (Figure 8a, 8b), suggesting some brine contribution to dense-water formation in the Southern Ocean.

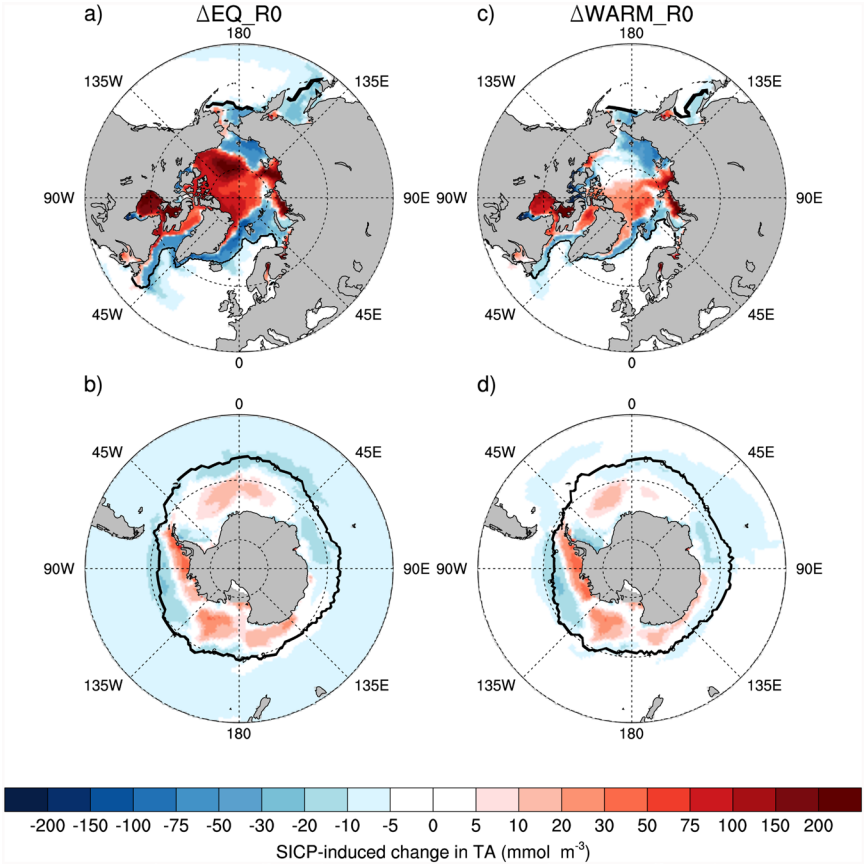

Figure 7

Simulated SICP-induced change in surface oceanic TA.

Annual mean SICP-induced change in TA (mmol m^{-3}) in the EQ_R0 experiment (a,b), and the WARM_R0 experiment (c,d). SICP-induced change in TA denotes the difference in TA between the SICP experiment (EQ_R0, WARM_R0) and the corresponding CTRL experiment (EQ_CTRL, WARM_CTRL), with a positive sign denoting that the SICP causes an increase in the oceanic TA concentration compared to the corresponding CTRL experiment (brine footprint), and a negative sign denoting a decrease in the oceanic TA concentration compared to the corresponding CTRL experiment (melt-water footprint). Surface layer is defined as the upper 12 m of the ocean. Black lines show the annual mean sea-ice margins. Latitudinal bands are shown for 80°, 60° and 40°. Results are averaged over the simulation years 451 to 500. Note that the color scale is nonlinear.

doi: 10.12952/journal.elementa.000136.f007

3.5.2 WARM scenario

As in the EQ scenario, the regional distribution of the annual mean surface ocean brine and melt-water footprints in the WARM scenario are mainly determined by the annual net sea-ice growth and melt (Figure 3c, 3d; Figure 7c, 7d). Considerably reduced annual net sea-ice growth in the Beaufort Sea strongly reduces the brine footprint in the WARM scenario compared to the EQ scenario (Figure 7c). The retreat of the sea-ice margin towards the north and reduced sea-ice import and melt in the Greenland and Labrador Seas (Figure 3c) in the WARM scenario (Figure 3c) lead to a considerably lower melt-water footprint compared to the EQ scenario in these seas (Figure 7c). In the Antarctic, both the brine and melt-water footprints in the WARM scenario are reduced compared to the EQ scenario (Figure 7d), resulting from the reduced annual sea-ice production (Figure 2d).

On a zonal mean, at depth the brine footprint in the Arctic Ocean is reduced and reaches to shallower depths (about 200 m) in the WARM compared to the EQ scenario (Figure 8c). This reduction is caused by reduced net sea-ice growth in the central Arctic Ocean (Figure 3c), and downwelling of the melt-water footprint in the center of the Beaufort Gyre (Figure 7c). The water spreading southward in the North Atlantic Ocean (south of 63°N and to a depth of 3000 m) is characterized by a melt-water footprint similar to the EQ scenario (Figure 8c). This similarity indicates that the reduced sea-ice melt in the Greenland and Labrador Seas (Figure 3c) is in the WARM scenario roughly compensated by the reduced southward transport of water and brine (Figure 6) in the WARM scenario. In the Antarctic, the reduced annual production of sea ice (Figure 2d), and hence of brine, and the reduced strength of the global meridional overturning circulation adjacent to Antarctica and below 3000 m depth (Figure 5c) result in a reduced brine footprint in the deep Southern, Pacific, and Indian Oceans in the WARM compared to the EQ scenario (Figure 8d).

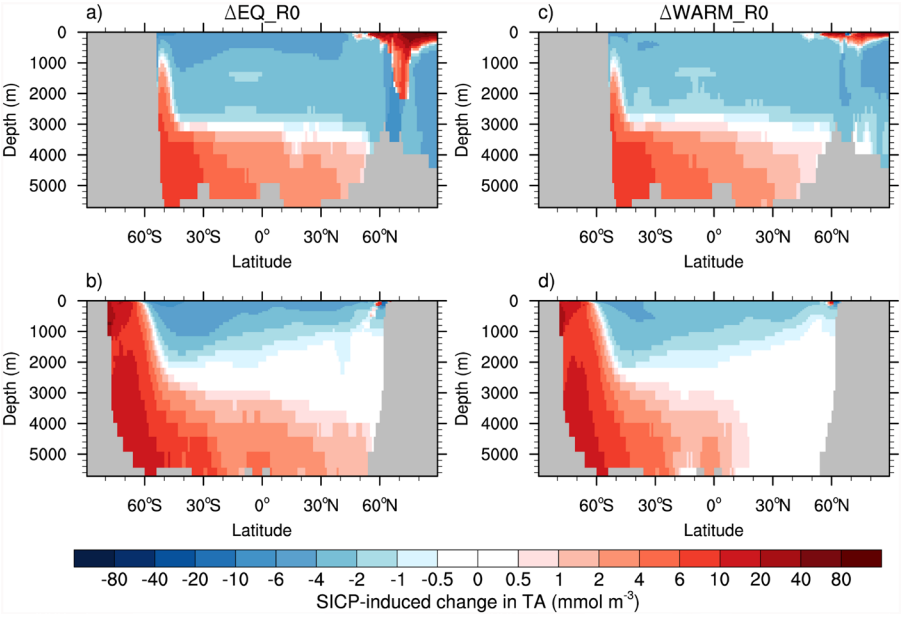

Figure 8

Simulated SICP-induced change in TA at depth.

Zonally averaged annual mean SICP-induced change in TA (mmol m^{-3}) in the EQ_R0 experiment (a,b), and the WARM_R0 experiment (c,d). SICP-induced change in TA denotes the difference in TA between the SICP experiment (EQ_R0, WARM_R0) and the corresponding CTRL experiment (EQ_CTRL, WARM_CTRL), with a positive sign denoting that the SICP causes an increase in the oceanic TA concentration (brine footprint), and a negative sign denoting a decrease in the CTRL oceanic TA concentration (melt-water footprint). Results are averaged over the Atlantic and Arctic Oceans (a,c), and zonally averaged over the Pacific, Indian and Southern Oceans (b,d), over the simulation years 451 to 500. Note that the color scale is nonlinear.

doi: 10.12952/journal.elementa.000136.f008

3.6 The SICP-induced air-sea CO_2 flux

We define a positive sign for a net CO_2 flux from the atmosphere to the ocean. SICP-induced air-sea CO_2 flux denotes the difference between the SICP experiments and the CTRL experiments (e.g., EQ_R0 minus EQ_CTRL), with a positive sign denoting that the SICP experiment shows more CO_2 uptake or less CO_2 out-gassing than its corresponding CTRL experiment, and vice versa for a negative sign. As one would expect from the temporally rather stable SICP-induced changes in surface ocean TA in both idealized climate scenarios (Figures S2 and S3), the simulated SICP-induced air-sea CO_2 fluxes are quasi-stationary after 150 years of simulation in the Arctic (Figures S4c, S4d and S5c, S5d), and after 400 to 450 years in the Antarctic (Figures S4b and S5b). The SICP-induced air-sea CO_2 flux is quantified by averaging the results over the simulation years 451 to 500.

3.6.1 The EQ climate scenario

The regional distribution of the SICP-induced air-sea CO_2 exchange in both hemispheres is broadly determined by the regional distribution of surface brine and melt-water footprints on both annual (Figures 7a, 7b and 9c–9f,) and seasonal scales (Figures S6a–S6d and S7e–S7l). Over most areas of the Arctic and Antarctic, an increased brine footprint in the surface ocean leads to a SICP-induced CO_2 out-gassing, whereas an increased melt-water footprint results in a SICP-induced oceanic CO_2 uptake. A large TA:DIC ratio of 2 prescribed in the sea ice (EQ_R2h versus EQ_R0) strengthens the SICP-induced air-sea CO_2 exchange, with the regional flux patterns remaining the same (Figures 9c–9f and S7e–S7l).

The strength of the SICP-induced air-sea CO_2 exchange, however, is not always just linearly related to the brine or melt-water footprint at the ocean surface. For example, in the Beaufort Gyre the annual mean SICP-induced oceanic CO_2 out-gassing is relatively small (Figure 9c, 9e), but the annual mean brine content is large (Figure 7a). This difference is because in the Beaufort Sea the almost complete winter sea-ice cover inhibits air-sea CO_2 exchange (Figure S7c, S7g, S7k), while the reduced summer sea-ice cover combined with a high surface brine footprint (Figure S6a) leads to an enhanced SICP-induced CO_2 out-gassing during summer (Figure S7e, S7i). This difference demonstrates that the annual SICP-induced CO_2 out-gassing in the Beaufort Sea (Figure 9c, 9e) is dominated by the summer conditions with reduced brine footprint and reduced sea-ice coverage compared to winter (Figure S6a, S6c).

Beyond the sea-ice margin in the North Atlantic Ocean (45°N–62°N, 45°W–8°W), an enhanced SICP-induced oceanic CO_2 out-gassing is simulated (Figures 9c, 9e and S7e, S7g, S7i, S7k). This SICP-induced out-gassing is caused by intensive mixing (Figure 4a) and entrainment of brine from below.

In both the Arctic and Antarctic sea-ice zones, the SICP-induced oceanic CO_2 uptake increases in the experimental order of R1.1h < R1.1l < R0 < R2l < R2h (Table 2). This ordering indicates that during sea-ice melt a maximum dilution of the surface TA and DIC concentrations without changing the oceanic ratio (R0) increases the SICP-induced oceanic CO_2 uptake more strongly than the melt-water release of some concentration of TA and DIC with a ratio of 1.1 (R1.1h, R1.1l). Because the oceanic ratio is already 1.1, the R1.1h and R1.1l experiments do not change the oceanic TA:DIC ratio. In contrast, the dilution effect on the SICP-induced oceanic CO_2 uptake is overwhelmed by the melt-water release of a TA:DIC ratio of 2 (R0 < R2). For this sea-ice ratio of 2, the increase in the oceanic TA:DIC ratio is larger for higher concentrations of TA and DIC released upon melt (R2l < R2h).

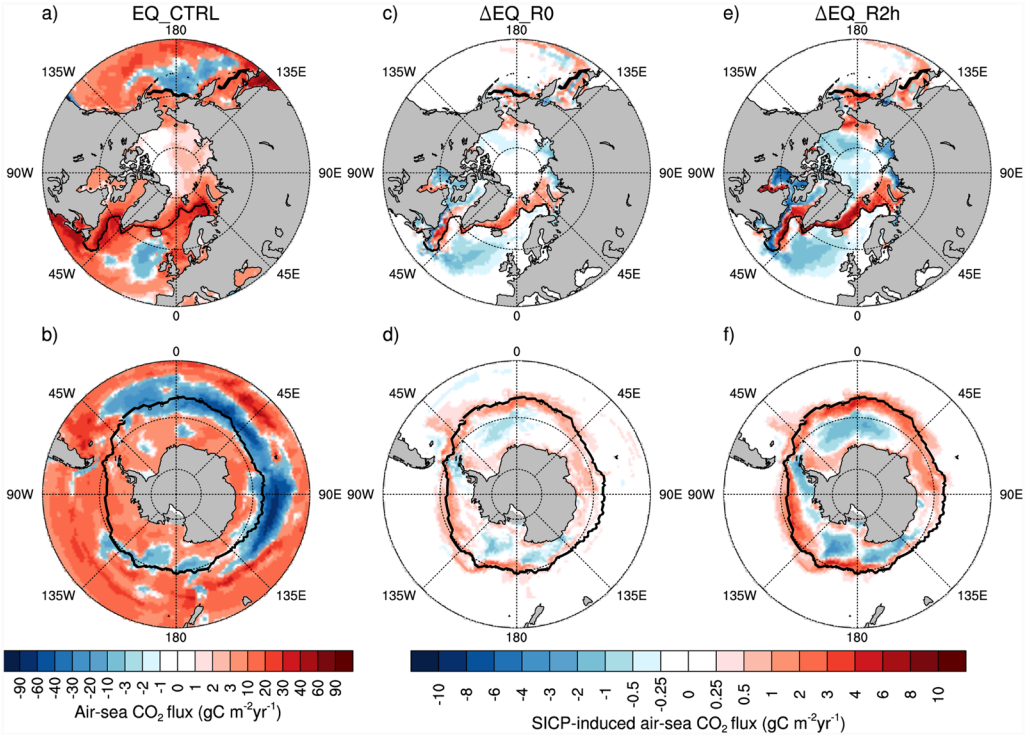

Figure 9

Simulated air-sea CO_2 flux and SICP-induced air-sea CO_2 flux in the EQ climate scenario.

Annual mean air-sea CO_2 flux (g C m^{-2} yr^{-1}) in the EQ_CTRL experiment (a,b), annual mean SICP-induced air-sea CO_2 flux (g C m^{-2} yr^{-1}) in the EQ_R0 experiment (c,d), and annual mean SICP-induced air-sea CO_2 flux in the EQ_R2h experiment (e,f) for the Arctic (a,c,e) and Antarctic (b,d,f) regions. The air-sea CO_2 flux in the EQ_CTRL experiment is positive for a net CO_2 flux from the atmosphere to the ocean (oceanic CO_2 uptake), and negative for the other direction (oceanic CO_2 out-gassing). SICP-induced air-sea CO_2 flux denotes the difference between the SICP experiment (EQ_R0, EQ_R2h) and the EQ_CTRL experiment, with a positive sign indicating that the SICP experiment shows more CO_2 uptake or less CO_2 out-gassing than the CTRL experiment; negative values indicate the opposite. Black lines show the annual mean sea-ice margins. Latitudinal bands are shown for 80°, 60° and 40°. Results are averaged over the simulation years 451 to 500. Note that the color scales are nonlinear.

doi: 10.12952/journal.elementa.000136.f009

Independent of the concentrations and ratios of TA:DIC prescribed in the sea ice, the SICP-induced oceanic CO_2 uptake in the Antarctic is larger than in the Arctic (Table 2). This difference is a consequence of the more efficient brine export away from the Antarctic mixed layer (Figure 8a, 8b; Section 3.7).

3.6.2 The WARM climate scenario

Similar to the EQ scenario, the magnitude of the SICP-induced air-sea CO_2 exchange in the WARM scenario is determined by the strength of the surface brine and melt-water footprints, with the regional patterns being enhanced for a larger concentration and ratio of TA and DIC prescribed in the sea ice (WARM_R0 versus WARM_R2h) (Figures 7c, 7d and 10c–10f). The larger summer melt-water footprint in the central Arctic Ocean compared to the EQ scenario (Figure S6e) causes an enhanced SICP-induced oceanic CO_2 uptake in the WARM scenario in summer (Figure S8e, 8i) and annually (Figure 10c, 10e; Table 2). The strength of the SICP-induced enhanced oceanic CO_2 uptake is reduced in the Greenland and Labrador Sea in the WARM compared to the EQ scenario (Figure 10c, 10e). This loss in strength is caused by the reduced sea-ice import and melt (Figure 3c), which reduces the melt-water footprint (Figure 7c). Similar to the EQ scenario, an

Table 2. Annual mean air-sea CO_2 flux and SICP-induced air-sea CO_2 flux by region and experiment[a]

Region	Area of region (m^2)		Air-sea CO_2 flux (Tg C yr^{-1})[b]		SICP-induced air-sea CO_2 flux (Tg C yr^{-1})[c]							
	EQ_CTRL	WARM_CTRL	EQ_CTRL	WARM_CTRL	ΔEQ_R0	ΔEQ_R2h	ΔEQ_R1.1h	ΔEQ_R2l	ΔEQ_R1.1l	ΔWARM_R0	ΔWARM_R2h	ΔWARM_R1.1l
Central Arctic Ocean[d]	1.02×10^{13}	1.02×10^{13}	46.1	83.6	0.2	0.0	0.2	0.2	0.2	1.2	3.8	1.3
Arctic sea-ice zone[e]	1.67×10^{13}	1.43×10^{13}	132.0	115.6	1.8	4.9	1.1	2.2	1.6	−0.5	1.6	0.0
North of 40°N	4.22×10^{13}	4.22×10^{13}	385.5	473.9	−0.1	2.7	−0.3	0.1	−0.3	−2.5	−1.1	−1.4
Antarctic sea-ice zone[e]	2.61×10^{13}	2.04×10^{13}	78.4	109.4	6.1	9.3	4.8	6.6	6.0	3.0	6.0	2.5
South of 40°S	7.67×10^{13}	7.67×10^{13}	274.9	302.8	11.1	15.1	8.5	11.7	10.9	5.5	9.1	4.3
Global	3.62×10^{14}	3.62×10^{14}	−325.1	321.6	16.3	20.7	11.3	16.8	15.5	6.7	10.1	5.1

[a]Experiment names as defined in Table 1.
[b]Positive values indicate net annual mean CO_2 flux from atmosphere to ocean (oceanic CO_2 uptake); negative values indicate the opposite direction (oceanic CO_2 out-gassing). Results are averaged over the simulation years 451 to 500; the temporal evolution of the air-sea CO_2 flux in these experiments is shown in Figure S9.
[c]Positive values indicate more CO_2 uptake or less CO_2 out-gassing in the SICP experiment than its corresponding control (CTRL) experiment; negative values indicate the opposite. Results are averaged over the simulation years 451 to 500; the temporal evolution of the SICP-induced air-sea CO_2 flux is shown in Figures S4 and S5.
[d]Regional extent is shown in Figure S10.
[e]Regional extent is defined as the annual mean sea-ice extent averaged over the years 451 to 500 (Figure 3).

doi: 10.12952/journal.elementa.000136.t002

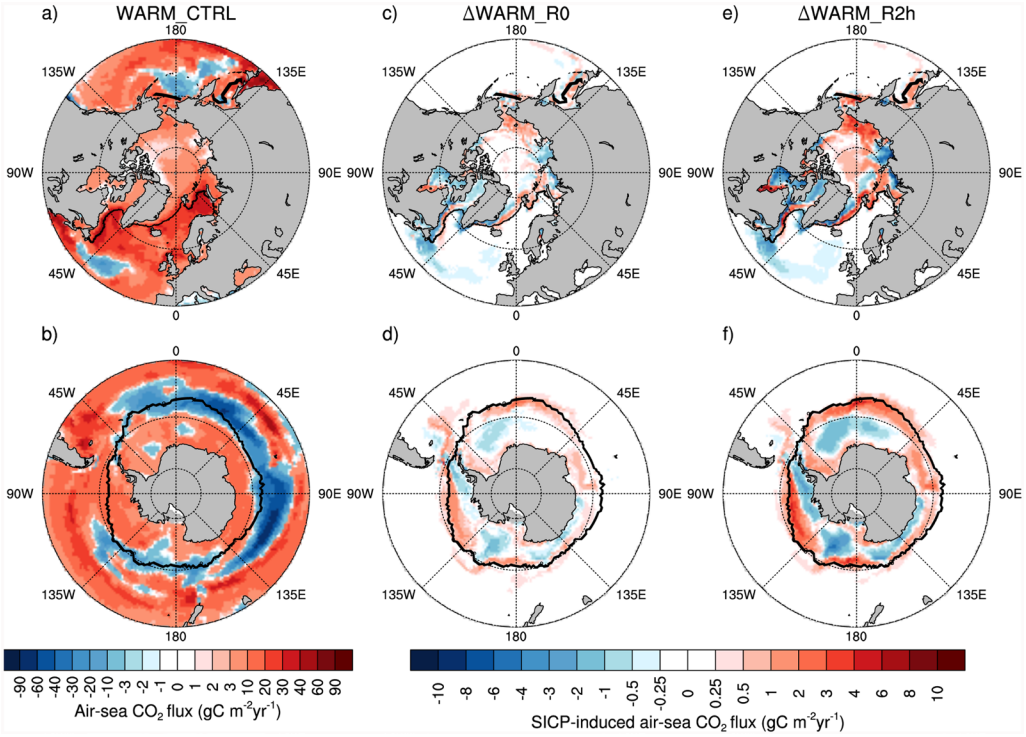

Figure 10

Simulated air-sea CO_2 flux and SICP-induced air-sea CO_2 flux for the WARM climate scenario.

Annual mean air-sea CO_2 flux (g C m^{-2} yr^{-1}) in the WARM_CTRL experiment (a,b), annual mean SICP-induced air-sea CO_2 flux (g C m^{-2} yr^{-1}) in the WARM_R0 experiment (c,d), and annual mean SICP-induced air-sea CO_2 flux in the WARM_R2h experiment (e,f) for the Arctic (a,c,e) and Antarctic (b,d,f) regions. The air-sea CO_2 flux in the WARM_CTRL experiment is positive for a net CO_2 flux from the atmosphere to the ocean (oceanic CO_2 uptake), and negative for the other direction (oceanic CO_2 out-gassing). SICP-induced air-sea CO_2 flux denotes the difference between the SICP experiment (WARM_R0, WARM_R2h) and the WARM_CTRL experiment, with a positive sign denoting that the SICP experiment shows more CO_2 uptake or less CO_2 out-gassing than the CTRL experiment; negative values indicate the opposite. Black lines show the annual mean sea-ice margins. Latitudinal bands are shown for 80°, 60° and 40°. Results are averaged over the simulation years 451 to 500. Note that the color scales are nonlinear.

doi: 10.12952/journal.elementa.000136.f010

enhanced SICP-induced oceanic out-gassing, caused by intensive mixing (Figure 4c) and brine footprint entrainment to the surface, is simulated in the North Atlantic Ocean south of the average sea-ice edge at 45°W-5°W/40°N-61°N (Figure 10c, 10e). The strength of this North Atlantic out-gassing is weaker in the WARM scenario than in the EQ scenario, which is related to the reduced North Atlantic southward water (and brine footprint) transport (Figure 6).

In contrast to the EQ scenario, in the WARM scenario the relative order of the Arctic SICP-induced oceanic CO_2 uptake rate is R0 < R1.1h < R2h (Table 2). This ordering shows that in the WARM scenario a low ratio of TA:DIC released upon sea-ice melt (R1.1h) increases the SICP-induced oceanic CO_2 uptake more strongly than a maximum surface ocean TA and DIC dilution upon sea-ice melt without changing the oceanic TA:DIC ratio (R0). This outcome is because in the WARM scenario, the Arctic surface ocean TA:DIC ratio is considerably lower than 1.1, which is mainly caused by the summer ice-free central Arctic Ocean allowing for an enhanced net oceanic CO_2 uptake compared to the EQ scenario (Table 2; Figure S9c). Consequently, the release of a low TA:DIC ratio of 1.1 upon sea-ice melt increases the oceanic TA:DIC ratio and induces an enhanced CO_2 uptake in the WARM scenario compared to the EQ scenario. In the Southern Ocean, TA:DIC ratios are around 1.1 both in the WARM scenario and in the EQ scenario. Hence, both scenarios have a similar order of the SICP-induced oceanic CO_2 uptake strength (R1.1h < R0 < R2h) (Table 2). As in the EQ scenarios, in the WARM scenario the SICP-induced oceanic CO_2 uptake is larger in the Antarctic than in the Arctic (Table 2), which is related to a more efficient brine export from the Antarctic than from the Arctic (Figure 8c, 8d; Section 3.7).

3.7 Estimation of the fraction of brine drainage below the polar mixed layer

In a conceptual view of the SICP, one would expect that in full equilibrium the additional CO_2 uptake caused by the SICP is out-gassed in non-polar regions in order to sustain the global flux balance. Thus, in equilibrium the mass of additional SICP-induced non-polar out-gassed CO_2 equals the mass of brine-associated DIC leaving the polar oceanic mixed layer. In our simulations, the global SICP-induced oceanic CO_2 flux balance (zero flux) is not established yet (Table 2). Nevertheless, because our simulations show a stable SICP-induced air-sea CO_2 exchange and brine or melt-water footprints in the sea-ice zones of both hemispheres (Figures S2, S3, S4b, S4d, and S5b, S5d), we can use this conceptual understanding to estimate the fraction of DIC that is transported away from the polar mixed layer.

In the EQ scenario, the model simulates an annual sea-ice production of $14.1 \cdot 10^{12}$ m^3 in the Arctic (Figure 2c). Based on this annual sea-ice production, we infer that the EQ_R0 experiment releases 300 Tg C yr^{-1} more brine-associated DIC to the surface ocean in the Arctic than the EQ_CTRL experiment (300 Tg C yr^{-1} = [2000 mmol DIC m^{-3} – 0 mmol DIC m^{-3}] · $14.1 \cdot 10^{12}$ m^3 yr^{-1} · [910 kg m^{-3} / 1025 kg m^{-3}] · 12 mg C $mmol^{-1}$ · 10^{-15} Tg mg^{-1}, where 910 kg m^{-3} denotes the sea-ice density, and 1025 kg m^{-3} denotes the seawater density). Assuming that the SICP-induced air-sea CO_2 flux (1.8 Tg C yr^{-1};

Table 2) equals the export flux of brine-associated DIC, we infer that 0.6% of the 300 Tg C of the brine-associated DIC produced every year leaves the Arctic mixed layer. In the Antarctic, about 3.1% of the annually produced brine-associated DIC is exported from the mixed layer. Performing this calculation for the SICP-induced air-sea CO_2 flux in the EQ_R2h experiment, we find a slight increase in the fraction of brine-associated DIC exported from the mixed layer, with values of 2.0% in the Arctic and 5.9% in the Antarctic. All other SICP experiments in the EQ scenario range between the two endmembers.

In the WARM climate scenario, we infer a brine-associated DIC export of –0.2% to 0.6% in the Arctic, with the lower estimate indicating net brine accumulation in the Arctic mixed layer. In the Antarctic, the brine-associated DIC export ranges between 1.9 and 4.7%.

4. Discussion

In this study we separate the mechanisms that influence the SICP-induced air-sea CO_2 flux. To do so, we have used a three-dimensional ocean-sea-ice-biogeochemical model and run a set of idealized SICP experiments combined with idealized climate scenarios. The SICP scenarios cover the range of observed TA and DIC compositions in the sea ice. The idealized climate scenarios (both forced with constant atmospheric CO_2 concentration) are designed to represent (i) the present-day ocean and sea-ice state (EQ scenario); and (ii) a future reduced oceanic overturning and Arctic sea-ice state (WARM scenario) that is comparable to the RCP4.5 scenario.

4.1 Mechanisms determining the strength of the SICP-induced air-sea CO_2 flux

Rysgaard et al. (2007) emphasize that the strength of the SICP-induced air-sea CO_2 flux is particularly sensitive to the fraction of brine being transported away from the polar mixed layer. Under the present-day strength of oceanic overturning (EQ scenario), the model-derived fractional export of brine-associated DIC ranges between 0.6 and 2% in the Arctic, and between 3.1 and 5.9% in the Antarctic. A reduction in the strength of the oceanic overturning circulation (WARM scenario) decreases the brine export to a maximum of 0.6% in the Arctic and 4.7% in the Antarctic. These differences in the fractions of brine-associated DIC export between the Arctic and Antarctic explain the larger SICP-induced oceanic CO_2 uptake in the Antarctic compared to the Arctic in both idealized climate scenarios. An earlier study using MPIOM (Stössel et al., 2002) has shown that sinking of dense water in the North Atlantic is rather insensitive to brine density. This insensitivity is confirmed by our model results showing that a relatively large brine footprint remains above the Arctic cold halocline, whereas the water spreading into the intermediate to deep North Atlantic contains more sea-ice melt-water than brine (Figure 8a, 8c). In contrast, dense-water sinking to depth in the Southern Ocean (in MPIOM) is to a larger extent driven by surface density changes induced by sea-ice brine drainage (Stössel et al., 2002). This effect is shown by the increased brine footprint in waters spreading from the Southern Ocean along the seafloor into the global ocean (Figure 8). In general, dense-water formation in global ocean general circulation models depends critically on the representation of mixing and of open water in the sea-ice cover (leads). Over leads, intense cooling and new-ice formation induce brine rejection that potentially contributes to the transport of dense water to depth. Hence, a model with higher resolution that more accurately resolves atmosphere-ocean interactions in leads and/or uses a different mixing parameterization might result in a stronger contribution of highly saline brine to dense-water formation, and hence a stronger SICP-induced oceanic CO_2 uptake.

On the regional scale, the SICP-induced air-sea CO_2 flux is largely determined by the cycle of sea-ice growth and melt, the oceanic circulation redistributing brine and sea-ice melt-water throughout the ocean, and the fraction of sea-ice coverage blocking the air-sea CO_2 exchange. Areas that are characterized by a distinct surface ocean brine footprint cause a SICP-induced oceanic CO_2 out-gassing. In contrast, surface ocean areas that are characterized by a melt-water footprint show an enhanced SICP-induced oceanic CO_2 uptake.

Both the concentrations of TA and DIC and the TA:DIC ratio prescribed in the sea ice relative to the basic oceanic TA and DIC setting further determine the strength of the SICP-induced CO_2 uptake, which is higher for high ratios of TA:DIC prescribed in the sea ice (R2l, R2h) than for low ratios (R1.1l, R1.1h). This general grouping of the experiments highlights the need for refined observations of bulk sea-ice TA and DIC concentrations both on the regional and seasonal scale. Such refined observations will then also allow for a more realistic representation of the SICP in global and regional models beyond the commonly used implementation of setting both TA and DIC to zero in the simulated sea ice.

Our results suggest that a retreat of the summer Arctic sea ice, as simulated in the WARM scenario, increases the SICP-induced oceanic CO_2 uptake over large areas of the central Arctic Ocean. Because the sensitivity towards changes in the TA and DIC concentrations and the TA:DIC ratio is increased under higher oceanic pCO_2 conditions (e.g., Sarmiento and Gruber, 2006), we expect that this SICP-induced oceanic CO_2 uptake in the central Arctic will be enhanced under the current rising atmospheric CO_2 concentrations.

4.2 Comparison of the simulated SICP-induced air-sea CO_2 flux to related studies

In a specific sea-ice melt region of the Greenland Sea (74°N–80°N, 15°W–0°E), the SICP-induced oceanic CO_2 uptake in summer (1 May to 1 September) reaches values of up to 12 g C m^{-2} yr^{-1} in the EQ_R2h scenario and 9 g C m^{-2} yr^{-1} in the WARM_R2h scenario. These fluxes are lower than the mean summer oceanic CO_2 uptake of 18 g C m^{-2} yr^{-1} of the SICP estimated from a simple model of melted sea ice in the mixed layer for the same season and region and a comparable SICP scenario (Rysgaard at al., 2009). This SICP-induced CO_2 flux in the EQ scenario constitutes around 30% of the present-day mean uptake in spring (45 ± 21 g C m^{-2} yr^{-1}) and summer (37 ± 14 g C m^{-2} yr^{-1}) in the Greenland Sea (Nakaoka et al., 2006). The simulated annual maximum for modeled SICP-induced oceanic CO_2 uptake in this region (74°N–80°N, 15°W–0°E) ranges between 13 and 28% of the observed uptake in the EQ scenario, and between 7 and 16% of the observed uptake in the WARM scenario. The observed uptake values used for these estimates are based on measurements of the annual present-day CO_2 flux from Nakaoka et al. (2006; mean of 52 ± 20 g C m^{-2} yr^{-1}) and Yasunaka et al. (2016; mean of 48 ± 13 g C m^{-2} yr^{-1}) derived from different regions in the Greenland Sea. Similarly, in other net sea-ice melt or growth regions, we find a considerable influence of the SICP-induced air-sea CO_2 flux on both the seasonal and annual scale.

Although the SICP considerably influences the high-latitude air-sea CO_2 flux, when averaged over the polar regions the SICP-induced CO_2 uptake only drives a small fraction of the net oceanic CO_2 uptake. This fraction is up to 4% for the Arctic and 12% for the Antarctic in the EQ scenario, dropping to 1% for the Arctic and 5% for the Antarctic sea-ice zone in the WARM scenario. In absolute numbers, the SICP drives a maximum polar oceanic CO_2 uptake of 14 Tg C yr^{-1} in the EQ scenario, and 8 Tg C yr^{-1} in the WARM scenario (Table 2), which is up to 7% of the simulated net polar oceanic CO_2 uptake. These values are lower than the derived estimates of 33 to 83 Tg C yr^{-1} assuming full brine export (Rysgaard et al., 2011), because considerable amounts of brine remain in the mixed layer in our experiments. The rather small SICP-induced variations between the climatic scenarios further demonstrate that changes in the physical ocean-sea-ice state barely influence the SICP-induced air-sea CO_2 flux when averaged over the polar regions. However, as discussed above, climatic changes induce considerable variations in the strength of the SICP on regional scales. For example, in the future summer sea-ice free central Arctic Ocean, the annual mean SICP-induced CO_2 uptake is likely to increase significantly.

An accompanying study simulating the SICP for pre-industrial climate conditions using a different global-ocean-sea-ice-biogeochemical model (NEMO-LIM-PISCES, Moreau et al., 2016) shows a similarly small fraction of brine transport away from the polar mixed layer, and similar regional patterns of the SICP-induced air-sea CO_2 flux that are also mainly determined by net sea-ice growth and melt areas. Compared to the current global oceanic net CO_2 uptake (mean of 2600 ± 500 Tg C yr^{-1}) which is forced by the rising atmospheric CO_2 concentrations (Le Quéré et al., 2015), the SICP-induced CO_2 uptake is small in the simulated idealized scenarios. However, for long term climatic changes, such as the transition between the last interglacial to glacial, which was accompanied by an increase in the sea-ice extent (Sarnthein et al., 2003; de Vernal et al., 2005; Gersonde et al., 2005), the SICP might have contributed to a significant drawdown of the atmospheric CO_2 concentrations. Indeed, using a model of intermediate complexity, Bouttes et al. (2010) show that a direct transport of brine to depth can explain a large part of the interglacial to glacial oceanic CO_2 uptake. In this case, the brine-associated DIC is transported directly from the surface to the deep ocean and the dense brine transported to depth stratifies the ocean, which are crucial for the long term trapping and accumulation of DIC in the deep ocean. To further constrain the influence of the SICP on the interglacial-glacial atmospheric CO_2 drawdown, simulations with an ocean-sea-ice-biogeochemical general circulation model resolving both regional circulation features and sea-ice dynamical processes are required.

5. Summary

Using a three-dimensional ocean-sea-ice-biogeochemical model for a set of SICP experiments within two idealized climate scenarios, we have separated the mechanisms that determine the strength of the SICP-induced air-sea CO_2 flux. The efficiency of the SICP itself is determined by the concentrations of TA and DIC and the TA:DIC ratio prescribed in the sea ice relative to the polar oceanic TA and DIC conditions; the efficiency of the SICP-induced oceanic CO_2 uptake is determined by the export of brine-associated DIC from the polar mixed layer to depth. Because that export to depth is larger in the Antarctic than in the Arctic, the SICP-induced oceanic CO_2 uptake is higher in the Antarctic. Particular uncertainties in the quantification of the SICP hence arise from modeling issues related to the sites and strength of dense-water formation and its transport throughout the ocean. Within the sea-ice zone, the strength and sign of the SICP-induced air-sea CO_2 exchange is controlled mainly by the relative distribution of brine produced during sea-ice formation (SICP-induced oceanic CO_2 out-gassing), and melt-water released during sea-ice melt (SICP-induced oceanic CO_2 uptake). These general air-sea CO_2 exchange features are modified further by the influence of sea-ice coverage on the air-sea CO_2 exchange.

Despite a minor role of the SICP in the modern global carbon cycle, the SICP-induced oceanic CO_2 uptake can be relatively large on the regional scale, which is the case, for example, in the Greenland Sea. Hence, representation of the SICP in regional models should be considered in order to accurately represent the regional pattern of air-sea CO_2 exchange. To further improve the accuracy of the simulated polar carbon cycle, enhanced measurement efforts refining sea-ice TA and DIC concentrations both on the regional and seasonal scales are required.

References

Bouttes N, Paillard D, Roche DM. 2010. Impact of brine-induced stratification on the glacial carbon cycle. *Clim Past* **6**: 575–589. doi: 10.5194/cp-6-575-2010.

de Vernal A, Eynaud F, Henry M, Hillaire-Marcel C, Londeix L, et al. 2005. Reconstruction of sea-surface conditions at middle to high latitudes of the Northern Hemisphere during the Last Glacial Maximum (LGM) based on dinoflagellate cyst assemblages. *Quat Sci Rev* **24**(7–9): 897–924. doi: 10.1016/j.quascirev.2004.06.014.

Dieckmann GS, Nehrke G, Papadimitriou S, Göttlicher J, Steininger R, et al. 2008. Calcium carbonate as ikaite crystals in Antarctic sea ice. *Geophys Res Lett* **35**(8): L08501. doi: 10.1029/2008GL033540.

Dieckmann GS, Nehrke G, Uhlig C, Göttlicher J, Gerland S, et al. 2010. Brief Communication: Ikaite ($CaCO_3{\cdot}6H_2O$) discovered in Arctic sea ice. *The Cryosphere* **4**: 227–230. doi: 10.5194/tc-4-227-2010.

Fransson A, Chierici M, Yager PL, Smith Jr WO. 2011. Antarctic sea ice carbon dioxide system and controls. *J Geophys Res-Oceans* **116**(C12035). doi: 10.1029/2010jc006844.

Geilfus N-X, Carnat G, Dieckmann GS, Halden N, Nehrke G, et al. 2013. First estimates of the contribution of $CaCO_3$ precipitation to the release of CO_2 to the atmosphere during young sea ice growth. *J Geophys. Res-Oceans* **118**(1): 244–255. doi: 10.1029/2012JC007980.

Gent PR, Willebrand J, McDougall TJ, McWilliams JC. 1995. Parameterizing eddy-induced tracer transports in ocean circulation models. *J Phys Oceanogr* **25**: 463–474. doi: 10.1175/1520-0485(1995)025<0463:PEITTI>2.0.CO;2.

Gersonde R, Crosta X, Abelmann A, Armand L. 2005. Sea-surface temperature and sea ice distribution of the Southern Ocean at the EPILOG Last Glacial Maximum—a circum-Antarctic view based on siliceous microfossil records. *Quat Sci Rev* **24**(7–9): 869–896. doi: 10.1016/j.quascirev.2004.07.015.

Gröger M, Mikolajewicz U. 2011. Note on the CO_2 air-sea gas exchange at high temperatures. *Ocean Model* **39**(3–4): 284–290. doi: 10.1016/j.ocemod.2011.05.003.

Heinze C, Maier-Reimer E. 1999. The Hamburg Oceanic Carbon Cycle Circulation Model version "HAMOCC2s" for longtime integrations. *Technical Report 20*. Hamburg: Deutsches Klimarechenzenrum/Modellberatungsgruppe.

Heinze C, Maier-Reimer E, Winguth AME, Archer D. 1999. A global oceanic sediment model for long-term climate studies. *Global Biogeochem Cy* **13**(1): 221–250. doi: 10.1029/98GB02812.

Hibler III WD. 1979. A dynamic thermodynamic sea ice model. *J Phys Oceanogr* **9**: 815–846. doi: 10.1175/1520-0485(1979)009<0815:ADTSIM>2.0.CO;2.

Ilyina T, Six KD, Segschneider J, Maier-Reimer E, Li H, et al. 2013. Global ocean biogeochemistry model HAMOCC: Model architecture and performance as component of the MPI-Earth system model in different CMIP5 experimental realizations. *J Adv Model Earth Syst* **5**(2): 287–315. doi: 10.1029/2012MS000178.

Jungclaus JH, Fischer N, Haak H, Lohmann K, Marotzke J, et al. 2013. Characteristics of the ocean simulations in the Max Planck Institute Ocean Model (MPIOM) the ocean component of the MPI-Earth system model. *J Adv Model Earth Syst* **5**(2): 422–446. doi: 10.1002/jame.20023.

Le Quéré C, Moriarty R, Andrew RM, Canadell JG, Sitch S, et al. 2015. Global Carbon Budget 2015. *Earth Syst Sci Data* **7**(2): 349–396. doi: 10.5194/essd-7-349-2015.

Levitus S, Boyer TP, Conkright ME, O'Brien T, Antonov J, et al. 1998: NOAA Atlas NESDIS 18,World Ocean Database 1998: VOLUME 1: INTRODUCTION. Washington, D.C.: U.S. Government Printing Office: 346 pp.

Loose B, Miller LA, Elliott S, Papakyriakou T. 2011. Sea ice biogeochemistry and material transport across the frozen interface. *Oceanography* **24**: 202–218. doi: 10.5670/oceanog.2011.72.

Maier-Reimer E, Kriest I, Segschneider J, Wetzel P. 2005. The Hamburg Ocean carbon cycle model HAMOCC5.1 - Technical description, Release 1.1. *Reports on Earth System Science*. Max-Planck-Institut für Meteorologie.

Marsland SJ, Bindoff NL, Williams GD, Budd WF. 2004. Modeling water mass formation in the Mertz Glacier Polynia and Adélie Depression, East Antarctic. *J Geophys Res* **109**(C11003). doi:10.1029/2004JC002441.

Marsland SJ, Haak H, Jungclaus JH, Latif M, Röske F. 2003. The Max-Planck-Institute global ocean/sea ice model with orthogonal curvilinear coordinates. *Ocean Model* **5**(2): 91–127. doi: 10.1016/S1463-5003(02)00015-X.

Meier W, Fetterer F, Savoie M, Mallory S, Duerr R, et al. 2011. NOAA/NSIDC climate data record of passive sea-ice concentration [Digital Media]. Boulder, Colorado: National Snow and Ice Data Center.

Moreau S, Vancoppenolle M, Bopp L, Aumont O, Madec G, et al. 2016. Assessment of the sea-ice carbon pump: Insights from a three-dimensional ocean-sea-ice biogeochemical model (NEMO-LIM-PISCES). *Elem Sci Anth* **4**: 000122. doi: 10.12952/journal.elementa.000122

Nakaoka S-I, Aoki S, Nakazawa T, Hashida G, Morimoto S, et al. 2006. Temporal and spatial variations of oceanic pCO_2 and air-sea CO_2 flux in the Greenland Sea and the Barents Sea. *Tellus B* **58**(2): 148–161. doi:10.1111/j.1600-0889.2006.00178.x.

Notz D, Haumann FA, Haak H, Jungclaus JH, Marotzke J. 2013. Arctic sea-ice evolution as modeled by Max Planck Institute for Meteorology's Earth system model. *J Adv Model Earth Syst* **5**(2): 173–194. doi: 10.1002/jame.20016.

Röske F. 2006. A global heat and freshwater forcing dataset for ocean models. *Ocean Model* **11**(3–4): 235–297. doi:10.1016/j.ocemod.2004.12.005.

Rysgaard S, Bendtsen J, Delille B, Dieckmann GS, Glud RN, et al. 2011. Sea ice contribution to the air–sea CO_2 exchange in the Arctic and Southern Oceans. *Tellus B* **63**(5) 823–830. doi: 10.1111/j.1600-0889.2011.00571.x.

Rysgaard S, Bendtsen J, Pedersen LT, Ramløv H, Glud RN. 2009. Increased CO_2 uptake due to sea ice growth and decay in the Nordic Seas. *J Geophys Res-Oceans* **114**(C09011). doi: 10.1029/2008JC005088.

Rysgaard S, Glud RN, Lennert K, Cooper M, Halden N, et al. 2012. Ikaite crystals in melting sea ice – implications for pCO_2 and pH levels in Arctic surface waters. *The Cryosphere* **6**(4): 901–908. doi: 10.5194/tc-6-901-2012.

Rysgaard S, Glud RN, Sejr MK, Bendtsen J, Christensen PB. 2007. Inorganic carbon transport during sea ice growth and decay: A carbon pump in polar seas. *J Geophys Res-Oceans* **112**(C03016). doi: 10.1029/2006JC003572.

Rysgaard S, Søgaard DH, Cooper M, Pućko M, Lennert K, et al. 2013. Ikaite crystal distribution in winter sea ice and implications for CO_2 system dynamics. *The Cryosphere* **7**: 707–718. doi: 10.5194/tc-7-707-2013.

Rysgaard S, Wang F, Galley RJ, Grimm R, Notz D, et al. 2014. Temporal dynamics of ikaite in experimental sea ice. *The Cryosphere* **8**: 1469–1478. doi: 10.5194/tc-8-1469-2014.

Sarmiento JL, Gruber N, 2006. *Ocean Biogeochemical Dynamics*, STU - Stud. Ed. Princeton University Press.

Sarnthein M, Pflaumann U, Weinelt M. 2003. Past extent of sea ice in the northern North Atlantic inferred from foraminiferal paleotemperature estimates. *Paleoceanography* **18**(1047). doi: 10.1029/2002PA000771.

Six KD, Maier-Reimer E. 1996. Effects of plankton dynamics on seasonal carbon fluxes in an ocean general circulation model. *Global Biogeochem Cy* **10**(4): 559–583. doi: 10.1029/96GB02561.

Steele M, Morley R, Ermold W. 2001. PHC: A Global Ocean Hydrography with a High-Quality Arctic Ocean. *J Climate* **14**: 2079–2087. doi: 10.1175/1520-0442(2001)014<2079:PAGOHW>2.0.CO;2.

Steiner NS, Christian JR, Six KD, Yamamoto A, Yamamoto-Kawai M. 2014. Future ocean acidification in the Canada Basin and surrounding Arctic Ocean from CMIP5 earth system models. *J Geophys Res-Oceans* **119**(1): 332–347. doi: 10.1002/2013JC009069.

Stössel A, Notz D, Haumann FA, Haak H, Jungclaus J, et al. 2015. Controlling high-latitude Southern Ocean convection in climate models. *Ocean Model* **86**: 58–75. doi: 10.1016/j.ocemod.2014.11.008.

Stössel A, Yang K, Kim S-J. 2002. On the role of sea ice and convection in a global ocean model. *J Phys Oceanogr* **32**: 1194–1208. doi: 10.1175/1520-0485(2002)032<1194:OTROSI>2.0.CO;2.

Wanninkhof R. 1992. Relationship between wind speed and gas exchange over the ocean. *J Geophys Res-Oceans* **97**(5): 7373–7382. doi: 10.1029/92JC00188.

Weiss RF. 1974. Carbon dioxide in water and seawater: The solubility of non-ideal gas. *Mar Chem* **2**(3): 203–215. doi: 10.1016/0304-4203(74)90015-2

Yasunaka S, Murata A, Watanabe E, Chierici M, Fransson A, et al. 2016. Mapping of the air–sea CO_2 flux in the Arctic-Ocean and its adjacent seas: Basin-wide distribution and seasonal to interannual variability. *Polar Science* **10**(3):323-334. doi: 10.1016/j.polar.2016.03.006.

Contributions

- Designed the model experiments: RG and DN
- Performed the model simulations, analyzed the data, wrote the first draft, coordinated and synthesized the contributions from the other authors: RG
- Discussed the results and contributed to writing the manuscript: RG, DN, RNG, SR, and KDS

Acknowledgments

This work is a contribution to the SCOR working group 140 on Biological Exchange Processes at Sea Ice Interfaces (BEPSII). We would like to thank the BEPSII members, in particular, Sebastien Moreau and Martin Vancoppenolle for the fruitful discussions about this study. We also would like to thank Uwe Mikolajewicz for his useful comments on the experimental design, and Lisa Miller and two anonymous reviewers for their very constructive comments that improved the manuscript. The model integrations were performed at the German Climate Computing Center (DKRZ).

Funding information

R. Grimm and D. Notz are funded by the Max-Planck Society within the Max Planck Research Group "Sea ice in the Earth system". R.N. Glud was supported by the commission for Scientific Research in Greenland (KVUG; GCRC6507) and the Danish Council for Independent Research (FNU; 0602-02276B). S. Rysgaard was funded by the Canada Excellence Research Chair (CERC) program. K.D. Six is funded by the Max-Planck Society through the Max Planck Institute for Meteorology's research group "Ocean biogeochemistry".

Competing interests

The authors declare no competing financial interests.

Supplemental material

Supplementary information accompanies this paper:

- **Text S1. Changes in the biological production**
- **Figure S1. Simulated SICP-induced change in POC flux.**
  Monthly mean SICP-induced change in POC flux (10^{-3} Tg C yr^{-1}) in 90 m depth averaged over the global ocean (a), the Antarctic sea-ice zone (b), the central Arctic Ocean (c), the Arctic sea-ice zone (d). SICP-induced change in POC flux denotes the difference between the SICP experiment (EQ_R0, EQ_R2h, WARM_R0, WARM_R2h) and the corresponding CTRL experiment (EQ_CTRL, WARM_CTRL), with a positive sign denoting that the SICP experiment shows an increased POC downward flux in its corresponding CTRL experiment. Regional extent of the central Arctic Ocean is shown in Figure S10, regional extent of the Arctic and Antarctic sea-ice zone as defined by the annual mean sea-ice extent (Figure 2). Results are averaged over the simulation years 451 to 500.
- **Figure S2. Simulated SICP-induced change in surface oceanic TA in the EQ_R0 experiment.**
  Surface layer is defined as the upper 12 m of the ocean. Results are annually averaged. SICP-induced change in TA (mmol m^{-3}) denotes the difference in TA between the SICP experiment (EQ_R0, EQ_R2h) and the EQ_CTRL experiment, with a positive sign denoting that the SICP causes an increase in the oceanic TA concentration compared to the EQ_CTRL experiment (brine footprint), and a negative sign denoting that the SICP causes a decrease in the oceanic TA concentration compared to the EQ_CTRL experiment (melt-water footprint).

- **Figure S3. Simulated SICP-induced change in surface oceanic TA in the WARM_R0 experiment.**
  Surface layer is defined as the upper 12 m of the ocean. Results are annually averaged. SICP-induced change in TA (mmol m^{-3}) denotes the difference in TA between the SICP experiment (WARM_R0, WARM_R2h) and the WARM_CTRL experiment, with a positive sign denoting that the SICP causes an increase in the oceanic TA concentration compared to the WARM_CTRL experiment (brine footprint), and a negative sign denoting that the SICP causes a decrease in the oceanic TA concentration compared to the WARM_CTRL experiment (melt-water footprint).
- **Figure S4. Simulated SICP-induced air-sea CO_2 flux in the EQ scenario.**
  Annual mean SICP-induced air-sea CO_2 flux (Tg C yr^{-1}) averaged over the global ocean (a), the Antarctic sea-ice zone (b), the central Arctic Ocean (c), and the Arctic sea-ice zone (d). SICP-induced air-sea CO_2 flux denotes the difference between the SICP experiment (EQ_R0, EQ_R2h) and the EQ_CTRL experiment, with a positive sign denoting that the SICP experiment shows more CO_2 uptake or less CO_2 out-gassing than the CTRL experiment. Regional extent of the central Arctic Ocean as shown in Figure S10, regional extent of the Arctic and Antarctic sea-ice zone as defined by the annual mean sea-ice extent (Figure 2). The dotted black horizontal line indicates the zero-line for SICP-induced air-sea CO_2 flux. Note the different y-axis scales.
- **Figure S5. Simulated SICP-induced air-sea CO_2 flux in the WARM scenario.**
  Annual mean SICP-induced air-sea CO_2 flux (Tg C yr^{-1}) averaged over the global ocean (a), the Antarctic sea-ice zone (b), the central Arctic Ocean (c), and Arctic sea-ice zone (d). SICP-induced air-sea CO_2 flux denotes the difference between the SICP experiment (WARM_R0, WARM_R2h) and the WARM_CTRL experiment, with a positive sign denoting that the SICP experiment shows more CO_2 uptake or less CO_2 out-gassing than the CTRL experiment. Regional extent of the central Arctic Ocean as shown in Figure S10, regional extent of the Arctic and Antarctic sea-ice zone as defined by the annual mean sea-ice extent (Figure 2). The dotted black horizontal line indicates the zero-line for SICP-induced air-sea CO_2 flux. Note the different y-axis scales.
- **Figure S6. Simulated SICP-induced change in surface oceanic TA.**
  Seasonal mean SICP-induced change in TA (mmol m^{-3}) in the EQ_R0 experiment (a-d), and the WARM_R0 experiment (e-h). SICP-induced change in TA implies the difference in TA between the SICP experiment (EQ_R0, WARM_R0) and the corresponding CTRL experiment (EQ_CTRL, WARM_CTRL), with a positive sign denoting that the SICP causes an increase in the oceanic TA concentration compared to its corresponding CTRL experiment (brine footprint), and a negative sign denoting a decrease in the oceanic TA concentration compared to its corresponding CTRL experiment (melt-water footprint). Results are averaged over the summer months MJJAS (a,e) and NDJFM (b,f), and averaged over the winter months NDJFM (c,g) and MJJAS (d,h). Superimposed is the sea-ice concentration with cross-shaded areas showing > 0.95, squared areas > 0.5, and dotted areas > 0. Surface layer is defined as the upper 12 m of the ocean. Latitudinal bands are shown for 80°, 60° and 40°. Results are averaged over the simulation years 451 to 500. Note that the color scales are nonlinear.
- **Figure S7. Simulated air-sea CO_2 flux and SICP-induced air-sea CO_2 flux in the EQ scenario.**
  Seasonal mean air-sea CO_2 flux (g C m^{-2} yr^{-1}) in the EQ_CTRL experiment (a-d), SICP-induced air-sea CO_2 flux (g C m^{-2} yr^{-1}) in the EQ_R0 experiment (e-h), and SICP-induced air-sea CO_2 flux in the EQ_R2h experiment (i-l). The air-sea CO_2 flux in the EQ_CTRL experiment is positive for a net CO_2 flux from the atmosphere to the ocean (oceanic CO_2 uptake), and negative for the other direction (oceanic CO_2 out-gassing). SICP-induced air-sea CO_2 flux denotes the difference between the SICP experiment (EQ_R0, EQ_R2h) and the EQ_CTRL experiment, with a positive sign denoting that the SICP experiment shows more CO_2 uptake or less CO_2 out-gassing than the CTRL experiment. First two rows show mean summer air-sea CO_2 flux and SICP-induced air-sea CO_2 flux (MJJAS (a,e,i), NDJFM (b,f,j)), and last two rows mean winter air-sea CO_2 flux and SICP-induced air-sea CO_2 flux (NDJFM (c,g,k), MJJAS (d,h,l)). Superimposed is the sea-ice fraction with cross-shaded areas showing > 0.95, squared areas > 0.5, and dotted areas > 0. Latitudinal bands are shown for 80°, 60° and 40°. Results are averaged over the simulation years 451 to 500. Note that the color scales are nonlinear.
- **Figure S8. Simulated air-sea CO_2 flux and SICP-induced air-sea CO_2 flux in the WARM scenario.**
  Seasonal mean air-sea CO_2 flux (g C m^{-2} yr^{-1}) in the WARM_CTRL experiment (a-d), SICP-induced air-sea CO_2 flux (g C m^{-2} yr^{-1}) in the WARM_R0 experiment (e-h), and SICP-induced air-sea CO_2 flux in the WARM_R2h experiment (i-l). The air-sea CO_2 flux in the WARM_CTRL experiment is positive for a net CO_2 flux from the atmosphere to the ocean (oceanic CO_2 uptake), and negative for the other direction (oceanic CO_2 out-gassing). SICP-induced air-sea CO_2 flux denotes the difference between the SICP experiment (WARM_R0, WARM_R2h) and the WARM_CTRL experiment, with a positive sign denoting that the SICP experiment shows more CO_2 uptake or less CO_2 out-gassing than the CTRL experiment. First two rows show mean summer air-sea CO_2 flux and SICP-induced air-sea CO_2 flux (MJJAS (a,e,i), NDJFM (b,f,j)), and last two rows mean winter air-sea CO_2 flux and SICP-induced air-sea CO_2 flux (NDJFM (c,g,k), MJJAS (d,h,l)). Superimposed is the sea-ice fraction with cross-shaded areas showing > 0.95, squared areas > 0.5, and dotted areas > 0. Latitudinal bands are shown for 80°, 60° and 40°. Results are averaged over the simulation years 451 to 500. Note that the color scales are nonlinear.
- **Figure S9. Simulated air-sea CO_2 flux.**
  Time series of the annual mean air-sea CO_2 flux (Tg C yr^{-1}) averaged over the global ocean (a), the area south of 40°S (b), the central Arctic Ocean (c), and the area north of 40°N (d). The air-sea CO_2 flux is positive for a net CO_2 flux from the atmosphere to the ocean (oceanic CO_2 uptake), and negative for the other direction (oceanic CO_2 out-gassing). Regional extent of the central Arctic Ocean as shown in Figure S10. Note the different y-axis scales.
- **Figure S10. Extent of the central Arctic Ocean.**
  Latitudinal bands are shown for 80°, 60° and 40°.

Data accessibility statement

The model code and data are available upon request under: publications@mpimet.mpg.de